Mon. Not. R. Astron. Soc. **000**, 1–13 (1994) Printed 1 February 2008 (MN LATEX style file v1.4)

Predicted Planck Extragalactic Point Source Catalogue

P. Vielva[1,2,⋆], E. Martínez-González[1], L. Cayón[1], J. M. Diego[1,2] J. L. Sanz[1] and L. Toffolatti[3]

[1] *Instituto de Física de Cantabria, Fac. Ciencias, Avda. Los Castros s/n, 39005, Spain*
[2] *Departamento de Física Moderna, Universidad de Cantabria, Avda. Los Castros s/n, 39005 Santander, Spain*
[3] *Departamento de Física, Universidad de Oviedo, c/ Calvo Sotelo s/n, 33007 Oviedo, Spain*

1 February 2008

ABSTRACT

An estimation of the number and amplitude (in flux) of the extragalactic point sources that will be observed by the Planck Mission is presented in this paper. The study is based on the Mexican Hat wavelet formalism introduced by Cayón et al. 2000. Simulations at Planck observing frequencies are analysed, taking into account all the possible cosmological, Galactic and Extragalactic emissions together with noise. With the technique used in this work the Planck Mission will produce a catalogue of extragalactic point sources above fluxes: 1.03 Jy (857 GHz), 0.53 Jy (545 GHz), 0.28 Jy (353 GHz), 0.24 Jy (217 GHz), 0.32 Jy (143 GHz), 0.41 Jy (100 GHz HFI), 0.34 Jy (100 GHz LFI), 0.57 Jy (70 GHz), 0.54 Jy (44 GHz) and 0.54 Jy (30 GHz), which are only slightly model dependent (see text). Amplitudes of these sources are estimated with errors below $\sim 15\%$. Moreover, we also provide a complete catalogue (for the point sources simulation analysed) with errors in the estimation of the amplitude below $\sim 10\%$. In addition we discuss the possibility of identifying different point source populations in the Planck catalogue by estimating their spectral indices.

Key words: methods: data analysis – techniques: image processing – cosmic microwave background

1 INTRODUCTION

The most accurate observations of the Cosmic Microwave Background (CMB) covering angular scales down to a few arcmins will be provided by the future ESA Mission: Planck (Mandolesi et al. 1998, Puget et al. 1998). Two instruments, the LFI (Low Frequency Instrument) and the HFI (High Frequency Instrument) will produce 10 maps of the sky at 9 frequencies ranging from 30 GHz to 857 GHz. High sensitivity together with high resolution will characterize these observations. Several emissions will contribute to the maps. The CMB signal and instrumental noise will be observed together with Galactic (free-free, synchrotron and dust emissions) and extragalactic foregrounds (extragalactic point sources and Sunyaev-Zel'dovich sources) in the Planck channels. One major concern is to develop methods to separate all these foregrounds from the cosmological signal. Several methods have already been proposed (Hobson et al. 1998, Bouchet et al. 1999, Baccigalupi et al. 2000) and there is a lot of work left to be done.

In this paper we focus on the extraction of extragalactic point sources from simulated Planck maps. Several methods have been developed to extract point sources from CMB maps as those presented in Hobson et al. 1999, Tegmark and Oliveira-Costa 1998 (TOC98, hereafter), Tenorio et al. 1999 and Cayón et al. 2000 (C00, hereafter). Hobson et al. based their work on Maximum Entropy Methods (MEM) to separate all the foregrounds in simulated Planck maps. They obtained residual maps in which instrumental noise plus extragalactic point sources were still presents. Point sources were finally extracted from the maps using SExtractor. TOC98 aimed to extract point sources from Planck data using a filter designed to amplify point source emissions by reducing the rms of other emissions. This method relies on the Gaussianity of the CMB and foregrounds and requires some knowledge about the power spectrum of each of the sources in a map. The last two papers present methods based on wavelets to extract point sources from microwave maps. More realistic simulations of the signals and point sources that will be observed in future microwave maps were used in C00. Moreover, the most important difference between the two wavelet based works is the wavelet used in the analysis. In a recent work, Sanz et al. 2000, show that the Mexican Hat wavelet (MHW hereafter) is the optimal pseudofilter to detect point sources in microwave maps, at least for a wide range of theoretical power spectra. It is also important to

⋆ e-mail: vielva@ifca.unican.es

notice that the method described in C00 does not introduce any assumptions about the nature of the CMB or other foregrounds.

This paper continues the method introduced in C00 to extract point sources from microwave maps. We present a complete study of Planck simulations (at all observing frequencies) to construct a Planck Extragalactic Point Source Catalogue. The paper is organized as follows. In Section 2 we describe the simulations to be used. The MHW formalism is briefly reviewed in Section 3, and a discussion about the optimal MHW scale to detect point sources in the different Planck channels is also included. The detection and flux estimation results are presented in Section 4. Section 5 includes a discussion on the possible estimation of spectral characteristics of different point source populations. Finally, the conclusions of this work are presented in Section 6.

2 PLANCK SIMULATIONS AT DIFFERENT FREQUENCIES

In order to predict how many extragalactic point sources will be observed in the Planck maps, we have simulated those maps including all the experimental constraints (given in Table 1) as well as all the emissions at each frequency. Although Planck will produce whole sky maps, we perform our analysis on squared regions of the sky of $12.8^\circ \times 12.8^\circ$. This procedure of dividing the celestial sphere in small, almost flat, patches does not imply any lost of generality since the scales relevant for the source detection are in the arcmin range. We restrict our analysis to regions outside the Galactic plane, defined by $-30^\circ < b < +30^\circ$. This sky cut is quite conservative and should be frequency dependent; for simplicity we will use the same cut for all maps. The total number of point sources to be observed by Planck will be given by the addition of the ones detected in squared regions covering a total area of 2π sr (half of the sphere).

The Galactic emission in the total area of the sky we analyse changes (depending on the observing frequency) from one squared region to another. To take into account the possible variations we have considered several representative squared regions characterized by different Galactic emission intensities. Specifically, we have studied ten different $12.8^\circ \times 12.8^\circ$ sky patches, each of them randomly chosen from each of the ten equally spaced intervals in which the dust emission (outside the Galactic cut) can be tentatively divided. We have chosen dust as the guide to divide the sky since it is clearly the dominant emission at high Planck frequencies. The other Galactic emissions are expected to be, in most of the sky outside the Galactic cut, below either CMB or dust emissions at all Planck frequencies. We have analysed the same ten patches at all Planck frequencies, and according to the results, we can distinguish four different zones in the 857 GHz channel, three in 545, 353 and 217 GHz channels, and just two in 143, 100, 70, 44 and 30 GHz channels. The characteristic values for each Galactic emission in these zones are given in Table 2. Thereby, six different patches can be assigned to Zone I at 857 GHz, two different ones at Zone II, and only one at both Zone III and Zone IV. At Zone I of the three next channels (545, 353 and 217) eight different patches can be assigned and only one at Zones II and III. Finally, at Zone I of the rest channels we assign nine different patches and just one at Zone II.

Frequency (GHz)	FWHM (arcmin)	Pixel size (arcmin)	σ_{noise} (10^{-6})
857	5.0	1.5	22211.10
545	5.0	1.5	489.51
353	5.0	1.5	47.95
217	5.5	1.5	15.78
143	8.0	1.5	10.66
100 (HFI)	10.7	3.0	6.07
100 (LFI)	10.0	3.0	14.32
70	14.0	3.0	16.81
44	23.0	6.0	6.79
30	33.0	6.0	8.80

Table 1. Experimental constrains at the 10 Planck channels. The antenna FWHM is given in column 2 for the different frequencies (a Gaussian pattern is assumed in the HFI and LFI channels). Characteristic pixel sizes are shown in column 3. The fourth column contains information about the instrumental noise level, in $\Delta T/T$ per pixel.

Dust emission have been simulated using the data and the model provided by Finkbeiner et al. 1999. This model assumes that dust emission is due to two components: a *hot* one with a mean dust temperature of ${T_D}^{hot} \simeq 16.2K$ and an emissivity $\alpha^{hot} \simeq 2.70$, and a *cold* one with a ${T_D}^{cold} \simeq 9.4K$, and an $\alpha^{cold} \simeq 1.67$.

Free-free emission is poorly known. Present experiments such as H-α Sky Survey [†] and the WHAM project [‡] will provide maps of H_α emission that could be used as a template for this emission. As a first approximation we have simulated the emission due to free-free using the correlation with dust emission in the way proposed by Bouchet et al. 1996.

Synchrotron emission simulations have been done using the all sky template provided by P. Fosalba and G. Giardino in the ftp site: *ftp://astro.estec.esa.nl*. This map is an extrapolation of the 408 MHz radio map of Haslam et al. 1982, from the original 1° resolution to a resolution of about 5 arcmin. A power law for the power spectrum with an exponent of -3 has been assumed. We have done an additional extrapolation to the smallest scale (1.5 arcmin) following the same power law. We include in our simulations the information on the changes of spectral index as a function of electron density in the Galaxy. This template have been done combining the Haslam map with the Jonas et al. 1998 at 2326 MHz and with the Reich & Reich 1986 map at 1420 MHz, and can be found in the previous ftp site.

We have also taken into account the possible Galactic emission due to rotational grains of dust, proposed by Draine & Lazarian 1998. This component could be important at the lowest frequencies of the Planck channels (30 and

[†] http://www.swarthmore.edu/Home/News/Astronomy/
[‡] http://www.astro.wisc.edu/wham/

Frequency (GHz)	Optimal Scale (R/σ_a)	Dust emission ($\Delta T/T$)	CMB emission ($\Delta T/T$)	Free-Free ($\Delta T/T$)	Synchrotron emissions ($\Delta T/T$)
857, Zone I	1.0	9.03×10^{-2} †	4.38×10^{-5}	6.91×10^{-5}	5.03×10^{-5}
857, Zone II	0.9	1.40×10^{-1} †	"	3.96×10^{-5}	1.73×10^{-5}
857, Zone III	0.8	5.48×10^{-1}	"	9.27×10^{-5}	8.30×10^{-5}
857, Zone IV	0.6	1.55	"	4.91×10^{-4}	2.37×10^{-5}
545, Zone I	1.3	6.94×10^{-4} †	4.38×10^{-5}	1.92×10^{-6}	1.56×10^{-6}
545, Zone II	0.9	4.54×10^{-3}	"	2.58×10^{-6}	2.46×10^{-6}
545, Zone III	0.6	1.22×10^{-2}	"	1.37×10^{-5}	7.63×10^{-7}
353, Zone I	1.2	3.67×10^{-5} †	4.38×10^{-5}	4.04×10^{-7}	3.63×10^{-7}
353, Zone II	1.0	2.54×10^{-4}	"	5.43×10^{-7}	5.49×10^{-7}
353, Zone III	0.7	6.54×10^{-4}	"	2.87×10^{-6}	1.85×10^{-7}
217, Zone I	0.9	3.25×10^{-6}	4.35×10^{-5}	2.71×10^{-7}	2.73×10^{-7}
217, Zone II	0.9	3.38×10^{-5}	"	3.64×10^{-7}	3.94×10^{-7}
217, Zone III	0.8	8.41×10^{-5}	"	1.92×10^{-6}	1.46×10^{-7}
143, Zone I	0.7	1.01×10^{-6}	4.21×10^{-5}	3.70×10^{-7}	4.11×10^{-7}
143, Zone II	0.7	2.55×10^{-5}	"	2.57×10^{-7}	2.28×10^{-7}
100 (HFI), Zone I	0.6	4.60×10^{-7}	4.05×10^{-5}	6.23×10^{-7}	7.49×10^{-7}
100 (HFI), Zone II	0.6	1.14×10^{-5}	"	4.23×10^{-6}	4.31×10^{-7}
100 (LFI), Zone I	0.8	4.59×10^{-7}	4.09×10^{-5}	6.24×10^{-7}	7.51×10^{-7}
100 (LFI), Zone II	0.8	1.13×10^{-5}	"	4.21×10^{-6}	4.32×10^{-7}
70, Zone I	0.8	2.32×10^{-7}	3.87×10^{-5}	1.18×10^{-6}	1.54×10^{-6}
70, Zone II	0.7	5.57×10^{-6}	"	7.77×10^{-6}	9.17×10^{-7}
44, Zone I	0.7	1.02×10^{-7}	3.43×10^{-5}	2.97×10^{-6}	4.17×10^{-6}
44, Zone II	0.7	2.28×10^{-6}	"	1.82×10^{-5}	2.60×10^{-6}
30, Zone I	0.6	5.26×10^{-8}	3.03×10^{-5}	6.53×10^{-6}	9.74×10^{-6}
30, Zone II	0.6	1.13×10^{-6}	"	3.84×10^{-5}	6.25×10^{-6}

Table 2. MHW optimal scales for the Planck channels in different Zones of the sky. The rms values of the Galactic and CMB emissions are also presented at each of the selected zones. †The dust amplitude intervals for these zones, in $\Delta T/T$, are: 5.54×10^{-2} – 1.35×10^{-1}, 857 GHz Zone I; 1.40×10^{-1} – 2.46×10^{-1}, 857 GHz Zone II; 4.33×10^{-4} – 1.03×10^{-3}, 545 GHz, Zone I; 2.31×10^{-5} – 5.46×10^{-5}, 353 GHz, Zone I.

44 GHz) in the outskirts of the Galactic plane, where it is around two times lower than the free-free emission. As the authors propose in that paper, this emission is correlated with the thermal dust one, through the neutral hydrogen column density (N_H):

$$I(\nu)_{rot} = f(\nu) N_H, \qquad I(3000\ GHz)_{thermal} = a N_H, \tag{1}$$

where $f(\nu)$ is the frequency dependence of the emissivity predicted by Draine & Lazarian and a is the correlation between the 21 cm emission and the infrared dust one. We addopt the correlation proposed by Boulanger & Pérault (1988):

$$a \approx 0.85 \times 10^{-14} Jy\ sr^{-1} \Big(\frac{H\ atoms}{cm^{-2}} \Big)^{-1}. \tag{2}$$

Hence, the rotational dust emission is simulated from the thermal one through the equation:

$$I(\nu)_{rot} = a^{-1} f(\nu) I(3000\ GHz)_{thermal}. \tag{3}$$

Sunyaev-Zel'dovich (SZ) effect simulations developed by Diego et al. 2000 have also been added to the maps. These simulations assume a flat ΛCMD Universe with $\Omega_m = 0.3$ and $\Omega_\Lambda = 0.7$. The CMB emission have been simulated for the same Universe, using the *Cl's* generated with the CMBFAST code (Seljak & Zaldarriaga, 1996).

Finally, the extragalactic point source simulations have been performed following the model of Toffolatti et al. 1998 (see their paper for more details) assuming the cosmological model indicated above.

3 MEXICAN HAT WAVELET METHOD: DETECTION AND AMPLITUDE ESTIMATION OF POINT SOURCES

Only recently have wavelet techniques been applied to analyze CMB maps. Among the different applications, they have been used to denoise CMB maps (Sanz et al. 1999a, 1999b, Tenorio et al. 1999), to detect non-Gaussianity (Ferreira et al. 1997, Hobson et al. 1999, Aghanim and Forni 1999) and, more recently, to detect and subtract point sources (C00, Tenorio et al. 1999).

We will study the detection of point sources in Planck simulated maps using the method introduced by C00. This method is based on the adequacy of the Mexican Hat to select point sources with a characteristic Gaussian shape introduced by the antenna beam. The MHW is an isotropic

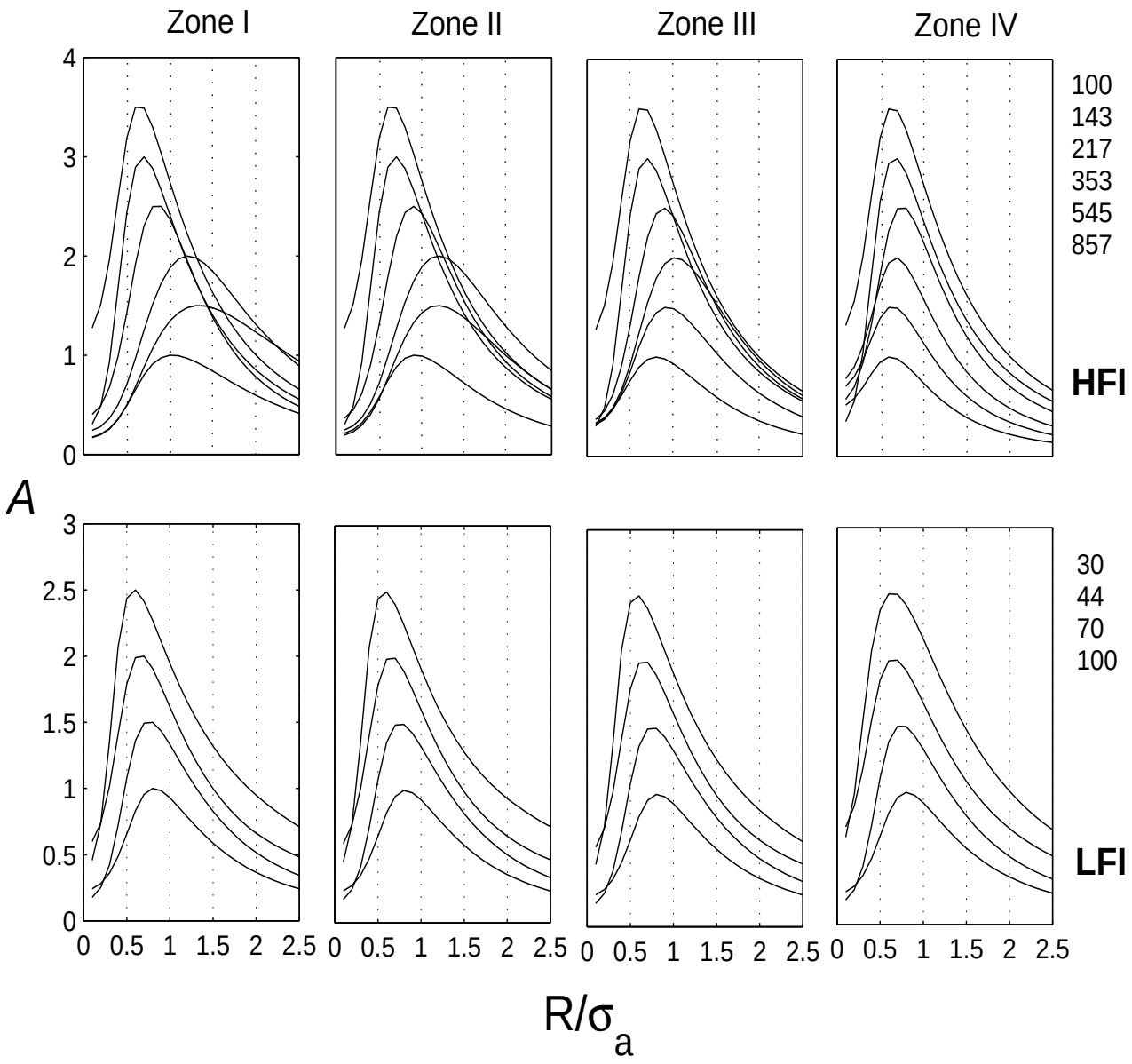

Figure 1. Amplification (arbitrary units) as a function of Mexican Hat scale in units of the antenna dispersion at each frequency, for different selected zones of the sky.

wavelet, characterized by a scale R. The analytical expression is given by

$$\psi(x) = \frac{1}{\sqrt{2\pi}}\left[2 - \left(\frac{x}{R}\right)^2\right] e^{-\frac{x^2}{2R^2}}. \quad (4)$$

Wavelet analyses are based on the study of the so called wavelet coefficients obtained by a convolution of the signal (a 2-D map in this case) being analyzed, with the wavelet. Thus, wavelet coefficient maps can be obtained at each characteristic scale R. In the case of a point source at position $\vec{x}_o$ of amplitude B and convolved with a Gaussian of dispersion σ_a, one can easily calculate the analytical expression of the wavelet coefficient:

$$\frac{w(R)}{R} = 2\sqrt{2\pi}\frac{B}{A}\frac{(R/\sigma_a)^2}{(1+(R/\sigma_a)^2)^2}, \quad (5)$$

where A is the area occupied by the point source (this is introduced for normalization purposes).

We are interested in detecting point sources from a background of CMB, noise and foreground emissions. The MHW increases the amplitude of the wavelet coefficients relative to the dispersion of the wavelet coefficient map $\sigma_w(R_{opt})$, at point source positions, at a certain optimal scale R_{opt}:

$$\frac{w(R_{opt})}{\sigma_w(R_{opt})} > \frac{(B/A)}{\sigma}, \quad (6)$$

where σ is the dispersion of the observed map (dispersion

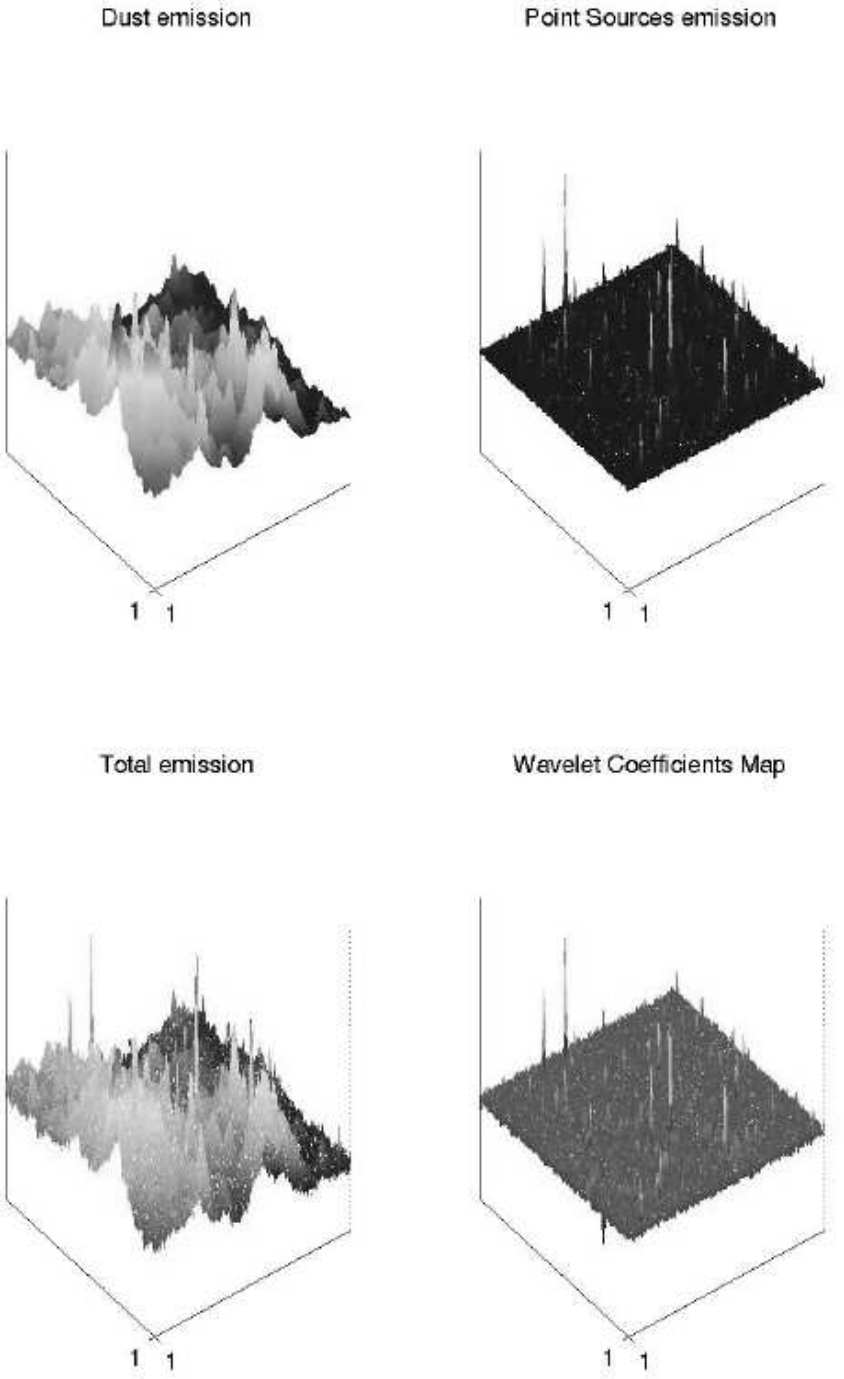

Figure 2. A graphical example of how the MHW works for one of our simulations at 857 GHz. The top left figure shows the dust emission. Point Sources are presented in the top right figure. The total emission, with all the Galactic and Extragalactic emissions, as well as the cosmological signal and the instrumental noise, is shown in the bottom left figure. The bottom right figure shows the wavelet coefficient map at the optimal scale.

in real space). The dispersion of the wavelet coefficients can be calculated from:

$$\sigma_w(R) = 2\pi R^2 \int dk P(k) k |\widehat{\psi}(Rk)|^2, \quad (7)$$

where $P(k)$ correspond to the power spectrum of the map to be analyzed and $\widehat{\psi}$ is the Fourier transform of the MHW. This together with the analytical expression of the wavelet coefficient allow us to estimate the amplification defined by:

$$\mathcal{A} \equiv \frac{w(R_{opt})\sigma}{(B/A)\sigma_w(R_{opt})}. \quad (8)$$

The amplification reaches its maximum value at the optimal scale. As it will be shown below, the optimal scale is defined by a combination of the characteristic scale and intensity of the foreground (or CMB background) that dominates the map and the amount of instrumental noise. We have calculated the optimal scale for each of the characteristic zones defined in the previous section at each frequency. The results are presented in Figure 1 and Table 2. Values of the optimal scale for each zone are given in that table. The variation of the optimal scale inside each zone is less than 5%.

As expected the optimal scale takes values around the antenna dispersion becuase this scale is the one that characterizes a point source. At low frequency the main emission is due to CMB. The typical CMB *coherence scale* is $\simeq 10'$, equal or smaller than the antenna dispersion at those frequencies. In this situation both point sources and background have similar variation scales (although the background characteristic scale will always be greater than the point source one). The optimal scale tends to be smaller than the antenna dispersion to better liminate the background contribution. Zones I and II at high frequencies will need optimal scales larger than σ_a to extract the point sources. This is due to the importance of noise relative to the dust emission. At zones strongly dominated by dust (Zones III and IV), although the background has a characteristic scale much larger than the antenna dispersion, however the optimal scale must be below σ_a. This is necessary to better erase the dust features (notice that in these zones the noise amplitude is much lower than the dust one, representing a minor problem). Therefore, the optimal scale on each map is a compromise between the background (its variation scale and its intensity) and the noise, in the sense that it tends to compensate for the effect of the most harmful contribution due to either the background or the noise.

We have plotted in Figure 2 an example of the effect of applying the MHW to a dust dominated map. At the optimal scale one can clearly see the point sources selected. Comparison of the two panels on the right gives a very good idea of how powerful the MHW is to detect point sources in those maps.

Once the optimal scale is calculated, we perform the point source detection on the corresponding wavelet map. We select k positions with wavelet coefficient $w(R_{opt})$ values larger than a certain threshold. Moreover, to make sure that the detection is a point source we fit the "experimental" $w(R, \vec{x}_o)$ versus R curve (obtained from the simulations) to the expected theoretical value given by eq. (5). In this paper we improve the χ^2 method used in C00. Correlations between the points in that curve were ignored in C00. To take this into account we define the χ^2 at pixel k by

$$\chi^2{}_k = \sum_{i,j} ({w_{i,k}}^{theo} - {w_{i,k}}^{exp}) {V_{i,j}}^{-1} ({w_{j,k}}^{theo} - {w_{j,k}}^{exp}), \quad (9)$$

where $V_{i,j}$ are elements of the covariance matrix between the different scales (i, j) and ${w_{i,k}}^{exp}$ and ${w_{i,k}}^{theo}$ represent the experimental and theoretical values of the wavelet coefficients of the selected pixels (k) at scale i. The covariance between scales i and j is given by

$$V_{ij} = \frac{1}{N} \sum_{k=1}^{N} {w_{i,k}}^{exp} {w_{j,k}}^{exp}, \quad (10)$$

where N is the number of wavelet coefficients at each scale (the number of pixels in the map). On our analysis we use a four scales fit, so $\mathbf{V}$ is a 4×4 matrix. This is an approximated covariance matrix, since it should be formed by the *noise* wavelet coefficients. Here, the *noise* must be understood as all the components except the point source which is being fitted. But our aim is, precisely, to estimate this point source. Hence, we are not able to determine, a priori, the point source contribution to that coefficient. However, the covariance matrix deffined by eq. (10) is approximately the exact one, since the contribution of each individual point source wavelet coefficient to the covariance matrix is negligible.

Two different criterions will be applied. In the first one, only pixels above $5\sigma_w(R_{opt})$ in the wavelet map at R_{opt} and with acceptable reduced χ^2 fits will be the ones selected. Taking into account our simulations, a reduced χ^2 is acceptable if it is lower or equal than 4. However, we accept a detection with a reduced χ^2 greater than the previous value if this detection appears in an adjacent channel with an acceptable reduced χ^2. This allows us to include in our catalogue some detections with low errors but without a total satisfactory fit. The amplitude of the point sources detected in this way is calculated from this fit. The second criterion is based on the error in the amplitude estimation. We look for those flux limits such that the errors are $\leq 50\%$ with a maximum percentage of spurious detections (i.e. error $> 50\%$) lower than 5%. We consider only wavelet coefficients above $2\sigma_w(R_{opt})$. As in the first criterion, we determine the amplitude from the fitted profile. We use a maximum χ^2 limit as in the previous criterion, with the same exception. We have applied these criterions to Planck simulations (described in Section 2) to generate the point source catalogues described in the following section.

4 POINT SOURCE CATALOGUE

Taking into account the number of different squared regions that are in the area of the sky analysed (outside the Galactic plane), we present in this Section the results of applying the MHW method (and the two different criterions) to obtain point source catalogues from the simulated Planck maps. We present two Tables for each criterion: one with the lowest fluxes achieved and other with the 100% completeness fluxes.

Point Source detections in 2π sr. $5\sigma_w(R_{opt})$ criterion.

Frequency (GHz)	$N(>5\sigma_{wc})$	% Bad detections	$\overline{E}_{abs}(\%)$	$\overline{E}(\%)$	Ampl.	Min flux (Jy)	% Detections	$N(>5\sigma_{rs})$
857	9408	1.5	9.9	-4.6	31.50	1.03	38.0	1907 (734)
545	2427	3.7	13.8	-8.9	17.44	0.53	33.5	1900 (445)
353	1088	2.6	14.3	-7.2	5.20	0.28	72.7	654 (250)
217	605	0.2	9.0	-4.1	6.85	0.24	74.5	26 (0)
143	651	0.1	9.5	-0.9	5.01	0.32	53.9	23 (16)
100 (HFI)	600	0.3	8.2	-4.4	3.62	0.41	58.9	6 (0)
100 (LFI)	486	0.1	11.3	-4.7	3.31	0.34	51.8	44 (39)
70	358	0.3	9.3	-2.8	2.84	0.57	87.3	5 (0)
44	350	0.5	10.9	-5.8	2.80	0.54	50.2	13 (5)
30	364	0.6	14.4	-9.6	2.95	0.54	51.7	18 (6)

Table 3. The frequency of each Planck channel is indicated in column 1. The second column shows the estimation of the number of detections above $5\sigma_w(R_{opt})$. The percentage of spurious detections with an error in the amplitude estimation $> 100\%$ (those spurious detections are generally contaminated by noise) is given in the third column. The absolute and real values of the mean error associated to the amplitude estimation are shown in columns 4 and 5. The mean amplification as defined in (8) is given in column 6. The seventh column shows the minimum flux reached. The percentage of point sources detected out of the total number of point sources present in the simulation is given in column 7. For comparison, the number of detections above $5\sigma_{rs}$ in the observed maps (real space) are shown in column 9. Numbers in brackets indicate the number of real point sources out of the total detected (σ_{rs} $(\Delta T/T) = 1.13$ (857 GHz), 8.51×10^{-4} (545 GHz), 6.28×10^{-5} (353 GHz), 4.37×10^{-5} (217 GHz), 4.21×10^{-5} (143 GHz), 4.05×10^{-5} (100 GHz, HFI), 4.09×10^{-5} (100 GHz, LFI), 3.87×10^{-5} (70 GHz), 3.46×10^{-5} (44 GHz), 3.18×10^{-5} (30 GHz)).

4.1 First criterion: $5\sigma_w(R_{opt})$

In Table 3, we give the results achieved with this criterions, for the lowest fluxes we are able to reach. The total number of point sources detected at each of the 10 Planck channels is given in the second column. We just detect the point sources in the tail of the flux number counts. We assume poissonian error bars for the number of point source detections. This is justified since for a given point source realization the difference in the number of detections from one $12.8^\circ \times 12.8^\circ$ patch of the sky to another in the same zone is much smaller than the poissonian error. The percentage of spurious detections is indicated in the third column. Though spurious detection are included in the number of detected sources, they are not in columns refering to the error and flux columns. These few "bad detections" are low amplitude point sources located at pixels with large noise fluctuations. The point source is correctly located by the MHW method but its estimated amplitude has a large error, $> 100\%$. As the table shows, this tends to happen less often at low frequencies where only the higher amplitude point sources are detected. In any case, the percentage of these "bad detections" is small at all frequencies ($< 4\%$). The fourth column in Table 3 shows that the mean absolute error in the amplitude estimation is always $< 15\%$. The fifth column shows that there is a slight bias in the amplitude estimation that tends to overestimate it. This method is based on the amplification of the ratio $w(R_{opt})/\sigma_w(R_{opt})$ relative to that ratio in real space. As can be noticed from the sixth column in Table 3, the amplification is usually larger at high frequencies where dust is the dominating foreground. All the detections presented in Table 3 are above the flux levels indicated in column 7. Out of all the point sources existing in the maps above those fluxes, the percentage detected is indicated in column 8. For comparison we give in the last column of Table 3 the number of point sources that will be detected in the original simulated maps by selecting all the pixels above 5σ, where σ is the *rms* value of a $12.8^\circ \times 12.8^\circ$ patch. Out of these pixels selected, only the ones given within parenthesis are real point sources. One has to take into account that there could be maps with large gradients that will have large σ values and will therefore not allow us to detect point sources above 5σ, even when they are visible.

It is also important to know the flux limit above which the *Planck Extragalactic Point Source Catalogue* will be complete. This information is provided in Table 4. The complete (100%) *Extragalactic Point Source Catalogue* will contain a maximum of $\simeq 5000$ point sources in the 857 GHz channel, and a minimum of 300 point sources in the 30 GHz channel. The error in the amplitude estimation is lower than 10% at all frequencies (except for the Zone II at 30 and 44 GHz, which represent $< 1\%$ of the sky outside the Galactic Plane).

4.2 Second criterion: 50% error

In Table 5, we present the catalogue of point source obtained above the lowest flux reached at each frequency. In the first column, we give the number of point sources detected at each channel. Results are extended to half of the sky. As explained above, we assume these number to have poissonian errors. The number of point sources detected are 2 to 3 times greater than the ones founded by the other criterion (since the $5\sigma_w(R_{opt})$ is quite conservative). In the second

Complete (100%) **Extragalactic Point Source Catalogue in** 2π **sr.** $5\sigma_w(R_{opt})$ **criterion.**

Frequency (GHz)	$N(>MinFlux)$	$\overline{E}_{abs}(\%)$	$\overline{E}(\%)$	Amplification	Min flux (Jy)	% Sky area
857, Zone I	4531	6.0	0.2	18.79	1.73	91.8
857, Zone II	296	5.9	0.4	42.09	1.83	6.2
857, Zone III	37	6.5	-0.3	56.95	2.18	1.0
857, Zone IV	0	–	–	–	–	1.0
857, Whole Sky	4864	6.0	0.2	20.63	1.74	
545, Zone I	1212	6.4	-0.5	6.25	0.99	98.0
545, Zone II	12	6.6	-2.2	44.63	1.13	1.0
545, Zone III	0	–	–	–	–	1.0
545, Whole Sky	1224	6.4	-0.5	6.64	0.99	
353, Zone I	646	9.2	0.3	4.08	0.41	98.0
353, Zone II	6	9.5	-0.4	61.6	0.42	1.0
353, Zone III	0	–	–	–	–	1.0
353, Whole Sky	652	9.2	0.3	4.66	0.41	
217, Zone I	466	7.2	-1.1	14.34	0.32	98.0
217, Zone II	5	7.2	-2.1	4.11	0.34	1.0
217, Zone III	2	5.6	-0.1	6.03	0.51	1.0
217, Whole Sky	473	7.2	-1.1	14.15	0.32	
143, Zone I	356	7.5	1.5	4.63	0.56	99.0
143, Zone II	4	6.9	1.4	5.76	0.61	1.0
143, Whole Sky	360	7.5	1.5	4.64	0.56	
100 (HFI), Zone I	417	6.0	-1.9	3.55	0.63	99.0
100 (HFI), Zone II	4	5.8	0.4	3.88	0.61	1.0
100 (HFI), Whole Sky	421	6.0	-1.9	3.55	0.63	
100 (LFI), Zone I	409	8.4	-2.2	3.35	0.64	99.0
100 (LFI), Zone II	5	7.2	-1.9	2.82	0.66	1.0
100 (LFI), Whole Sky	414	8.4	-2.2	3.34	0.64	
70, Zone I	327	9.1	-2.8	2.88	0.72	99.0
70, Zone II	4	9.4	-1.4	2.62	0.77	1.0
70, Whole Sky	331	9.1	-2.8	2.88	0.72	
44, Zone I	293	8.1	-2.4	2.87	0.81	99.0
44, Zone II	2	11.8	-1.4	2.62	1.02	1.0
44, Whole Sky	295	8.1	-2.4	2.87	0.81	
30, Zone I	295	9.5	-4.1	2.97	0.89	99.0
30, Zone II	2	26.6	-26.6	2.50	0.89	1.0
30, Whole Sky	297	9.7	-4.3	2.97	0.89	

Table 4. The number and characteristics of point sources in the complete (100%) catalogue are given in this table. Results are separated for the different sky zones. We also give an all sky estimation for the Complete Extragalactic Catalogue, taking into account the amount of sky that each Zone represent. Galactic emission increases from Zones I to IV (see Table 2). The number of point sources in the complete catalogue is indicated in the second column, these values have poissonian errors. Absolute and real values of the amplitude estimation mean errors are provided in columns 3 and 4. The mean amplification, as defined in (8), is given in column 5. Column 6 shows the minimum flux above which all point sources are detected. The last column gives an estimation of the percentage of the sky covered by each zone.

column, we give the number of spurious detections, fixed to be lower than 5% by the criterion. In this case, the percentage of "bad detections" is included in all the columns, since the errors are not so large than the ones in the other criterion. As in Table 3, the mean amplitude estimation errors are given in columns 4 and 5. The absolute error in the amplitude estimation is always lower than 16%. Actually, the mean error provided by this criterion is greater than the one from the first criterion, since we are detecting more sources with lower fluxes. The first criterion provide, in this sense, a *robust* catalogue. The flux limits and the percentage of simulated point sources above those fluxes is given in columns 6 and 7. The minimum fluxes achieved are, generally, lower than those obtained with the $5\sigma_w(R_{opt})$ criterion. The best improvement in the flux limit appears in the intermediate and low frequency channels. In these cases the number of point sources detected by the first criterion in each simulation (small patch) was very small (≤ 6). This means that we detect point sources in the tail of the flux distributions. The new criterion increases the number of detections which implies significant variations in the flux limits achieved. This

Point Source detections in 2π sr. 50% error criterion.

Frequency (GHz)	$N(>5\sigma_{wc})$	% Bad detections	$\overline{E}_{abs}(\%)$	$\overline{E}(\%)$	Min flux (Jy)	% Detections
857	24221	4.8	16.5	-9.4	1.05	85.2
545	3496	3.6	12.7	-4.6	0.63	74.5
353	1497	0	13.8	-3.4	0.26	95.0
217	1130	0	12.6	-0.5	0.17	95.0
143	1258	0	12.6	-2.9	0.18	90.9
100 (HFI)	1526	0	13.5	-5.9	0.19	80.8
100 (LFI)	1165	0	13.4	-4.6	0.26	77.1
70	1008	0	13.5	-8.2	0.30	88.9
44	990	0	15.3	-9.8	0.40	95.0
30	864	0	13.8	-8.8	0.49	100.0

Table 5. The frequency of each Planck channel is indicated in column 1. The second column shows the estimation of the number of detections with this criterion. The percentage of spurious detections with an error in the amplitude estimation $> 100\%$ (those spurious detections are generally contaminated by noise) is given in the third column. The absolute and real values of the mean error associated to the amplitude estimation are shown in columns 4 and 5. The minimum flux reached is shown in column 6. The percentage of point sources detected out of the total number of point sources present in the simulation is given in column 7.

is not the case for the 857, 545[§] and 353 GHz channels. The number of point sources detected with both methods gives a good determination of the detection level (an increment of detections does not change significantly the flux limit).

Finally, in Table 6 we present the complete (100%) *Extragalactic Point Source Catalogue* obtained with this criterion. It will contain a maximum of $\simeq 14000$ point sources in the 857 GHz channel and a minimum of $\simeq 800$ sources in the lowest frequency channels. The error in the amplitude estimation is lower than 15% except for the 44 GHz channel and Zone II at 30 GHz. Again, these errors are greater han the ones provided by the first criterion, whereas the number of point sources detected is greater and the completeness fluxes are lower. Another advantage of this method is that the division in Zones of the different parts of the sky are less important. That division into different Zones was due to the different amount of amplification of the point sources. However the second criterion does not depend so much on the amplification (the detection procedure requires only to be above $2\sigma_w(R_{opt})$ threshold).

Finally, the results obtained from both criterions are clearly model dependent, since we adopt a specific evolution model. However, if we change the evolution model for dusty galaxies, by adopting realistic models in agreement with current determinations of the diffuse far-IR/sub-mm back ground (FIRB), we still find source detection limits which are very similar to the quoted ones. For example, by using model E of Guiderdoni et al. (1998) the detection limit at 353 GHz does not change appreciably. Confusion noise from undetected sources is increased by a factor of ~ 3 but the dominant sources of noise at 353 GHz are still dust emission from our Galaxy and the CMB itself. On the other hand, the number of detected sources is obviously higher. At higher frequencies galactic dust emission dominates all the other noise sources even at high galactic latitudes (adopting the template of Finkbeiner et al., 1999; see Table 2), whereas at $\nu \leq 200$ GHz confusion noise from undetected sources is always below either CMB and galactic noise."

[§] In this channel, the minimum flux limit achieved in the first detection method is lower than in the second one. This is due to faint sources highly amplified and appears above $5\sigma_w$. These sources are too faint to be detected above the flux threshold determined by the second method

5 POINT SOURCE POPULATIONS: SPECTRAL INDEX ESTIMATION

A multifrequency analysis allows us to find point sources in coincidence at several frequencies. Assuming a certain frequency dependence for the intensity we can determine spectral indices characterizing the different point source populations that will be observed by Planck.

We model the frequency dependence of the point source intensity in a simple way

$$I = I_o \left(\frac{\nu}{\nu_o} \right)^{\alpha}, \tag{11}$$

being α the spectral index that will define the different point source populations.

In Table 7 we give an estimation of the number of point sources that are found in coincidence in different channels, using the $5\sigma_w(R_{opt})$ criterion data. By fitting the point source estimated amplitudes to the expression given above we calculate the spectral indices given in columns 6, 7 and 8. For comparison, the true values of these spectral indices are given in columns 3, 4 and 5. The mean errors are presented in the last column of Table 5. For spectral indices close to zero (flat spectrum) we give the absolute error, whereas for typical spectral indices of infrared galaxies relative errors are provided.

Complete (100%) **Extragalactic Point Source Catalogue in** 2π **sr.** 50% **error criterion.**

Frequency (GHz)	$N(> MinFlux)$	$\overline{E}_{abs}(\%)$	$\overline{E}(\%)$	Min flux (Jy)	% Sky area
857, Zone I	13089	11.1	-2.5	1.19	91.8
857, Zone II	781	10.8	-1.8	1.23	6.2
857, Zone III	77	10.3	-1.5	1.52	1.0
857, Zone IV	3	2.4	1.5	6.90	1.0
857, Whole Sky	13950	11.0	-2.4	1.25	
545, Zone I	2803	11.2	-2.5	0.67	98.0
545, Zone II	21	10.9	-3.5	0.73	1.0
545, Zone III	1	2.6	0.4	2.58	1.0
545, Whole Sky	2825	11.1	-2.4	0.69	
353, Zone I	1235	13.9	-1.9	0.28	98.0
353, Zone II	10	13.7	-1.8	0.30	1.0
353, Zone III	1	5.1	0.2	0.72	1.0
353, Whole Sky	1246	13.9	-1.9	0.28	
217, Zone I	998	12.9	1.6	0.19	98.0
217, Zone II	10	12.8	-0.1	0.19	1.0
217, Zone III	5	9.9	1.4	0.26	1.0
217, Whole Sky	1013	12.9	1.6	0.19	
143, Zone I	998	11.2	-1.1	0.23	99.0
143, Zone II	8	10.4	1.8	0.34	1.0
143, Whole Sky	1006	11.2	-1.1	0.23	
100 (HFI), Zone I	998	9.9	-3.5	0.36	99.0
100 (HFI), Zone II	9	9.6	-2.6	0.38	1.0
100 (HFI), Whole Sky	1007	9.9	-3.5	0.36	
100 (LFI), Zone I	1073	14.2	-3.9	0.31	99.0
100 (LFI), Zone II	10	14.2	-4.0	0.31	1.0
100 (LFI), Whole Sky	1083	14.2	-3.9	0.31	
70, Zone I	748	13.6	-6.4	0.37	99.0
70, Zone II	8	14.5	-7.5	0.37	1.0
70, Whole Sky	756	13.6	-6.4	0.37	
44, Zone I	873	16.2	-9.6	0.44	99.0
44, Zone II	4	9.2	-2.3	0.64	1.0
44, Whole Sky	877	16.1	-9.5	0.44	
30, Zone I	859	13.8	-8.7	0.49	99.0
30, Zone II	4	21.7	-19.5	0.77	1.0
30, Whole Sky	863	13.9	-8.8	0.49	

Table 6. This Table shows similar characteristics than the ones in Table 4. The number of point sources in the complete catalogue is indicated in the second column. Absolute and real values of the amplitude estimation mean errors are provided in columns 3 and 4. Column 5 shows the minimum flux above which all point sources are detected. The last column gives an estimation of the percentage of the sky covered by each zone.

As shown in Table 7, and in agreement with the input model, two main source populations can be identified in our catalogue of detected sources. Infrared selected sources – starburst and late type galaxies at intermediate to low redshift and high redshift ellipticals – with spectral indices close to ~ 2.5 are detected at high frequency. On the other hand, radio selected flat–spectrum AGNs (radio–loud quasars, blazers, etc.) are the dominant population in the low frequency channels. At intermediate frequencies (353, 217 and 143 GHz) the spectral index is ~ -0.5. The dominant source population in these frequencies (from the Toffolatti et al. 1998 model) is the infrared one, and it is so flat because the point source model has taken these frequencies as the ones where the dominant galaxy emission is turning from the dust emission to the synchrotron one. The choice of the turning frequency is highly model–dependent because of the poor knowledge of the galaxy emission at this spectral range. Future observations (as the Planck one) will help us to better determine the spectral behavior of point sources at these frequencies. In particular, to discriminate between flat–spectrum and infrared populations in these channels, we need to know more information in the adjacent ones.

Some point sources can be followed through three or more adjacent channels being the spectral index estimation quite good, with low errors. At high as well as at low frequencies, the knowledge of the spectral behaviour can help to increase the number of point sources detected.

Channels (GHz)	$\sim N(>5\sigma_w)$	α_{min}	$\overline{\alpha}$	α_{max}	${\alpha_{min}}^{est}$	$\overline{\alpha}^{est}$	${\alpha_{max}}^{est}$	Mean Error
857 – 545	2550	1.95	2.46	2.89	1.69	2.29	3.02	9.55%
857 – 545 – 353	810	2.49	2.71	3.09	2.38	2.64	3.09	4.21%
353 – 217 – 143	300	-0.52	-0.55	-0.58	-0.65	-0.49	-0.33	0.13
100 – 70	375	-0.17	-0.16	-0.15	-0.18	-0.04	0.12	0.13
70 – 44	375	-0.12	-0.10	-0.08	-0.36	-0.28	-0.16	0.18
44 – 30	300	0.07	0.08	0.09	-0.05	0.24	0.53	0.29
100 – 70 – 44 – 30	300	-0.07	-0.06	-0.05	-0.18	-0.14	-0.10	0.08

Table 7. Spectral indices for point sources found in coincidence at the frequencies indicated in column 1. An estimation of the number of point sources found in coincidence in the whole sky (outside the Galactic plane) is given in the second column. Third, fourth and fifth columns give minimum, mean and maximum values of the spectral indices as calculated from the original point source simulation. The spectral index estimation obtained from the MHW method is presented in columns 6, 7 and 8. The mean error in the spectral index estimation (absolute error for spectral index close to zero are given) is shown in the last column.

6 CONCLUSIONS AND DISCUSSION

The MHW method introduced in C00 to detect point sources in microwave maps has been revised and improved in this paper. We are able to establish the optimal Mexican Hat scale to maximize the detection of point sources. Moreover, the amplitude estimation is now based on a χ^2 estimator that takes into account the correlation between different scales. Using this method we have estimated the number and amplitude of point sources that will be detected over the whole sky (outside the Galactic plane) in any of the Planck channels. We provide information about all the point sources to be detected above a limiting flux as well as all the ones that will be part of a complete catalogue. We considered two different criterions to determine the point source catalogues. With the first one, we select those sources which are above $5\sigma_w(R_{opt})$ and have an optimal χ^2. With the second one, we select those sources which are above certain fluxes, such that the amplitude estimation error is $< 50\%$, allowing a 5% of spurious detections. Assuming the first criterion, the amplitude estimation errors are in all channels below 15%, whereas the second one provides a slightly worse estimation. On the other hand, the flux limits obtained with the last one are lower than the ones obtained with the first criterion (except for the highest channels, where the number of detections with both criterions are enough to determine the flux threshold).

It is important to notice that this *Planck Extragalactic Point Source Catalogue* will be directly obtained from the observed maps, without denoising them or separating the foregrounds. No assumption is needed about the nature of the signal and noise that will be present in the observed maps. The only assumption made in this work is the Gaussian and white nature of the instrumental noise. We have not tested how the presence of other kinds of noise can modify the results. However, it is expected that only correlated noise with a variation scale around the point source one would be a handicap to our method. In this case, a study with an optimal pseudofilter, in the manner proposed by Sanz et al., 2000 should be done. In that work the MHW detection method and the pseudofilter one are compared in presence of different kinds of noise. The results demonstrate that there are only small differences in the amplification achieved with the two filters.

The study here presented is done considering all the Planck channels. This allows us to look for point sources coincident in different frequency maps. A simple spectral dependence model is assumed and spectral indices are estimated for different populations present in the extracted *Planck Extragalactic Point Source Catalogue*. As discussed in the previous Section (and shown in Table 7), the proposed detection method is able to recognize the two main source populations present in the simulated maps as well as to give spectral index estimations with errors below 10%. Moreover, knowledge of spectral behaviour can be used to detect more point sources.

The MHW has proved to be the most powerful tool to extract point sources from microwave maps. Using information at different scales provides estimations of point source amplitudes with very small errors. The MHW method has advantages over the other methods also applied to microwave maps as explained in the Introduction. We have also done the exercise of comparing the MHW with the image analysis package SExtractor. We have analysed a square $12.8^\circ \times 12.8^\circ$ patch at 857 GHz. An especially optimal case for point source estimation has been chosen: a very low and homogeneous dust emission patch (belonging to Zone I with rms $= 5.99 \times 10^{-2}$, close to the lowest limit in this zone. See Table 2). We have studied different ways to detect and subtract point sources using SExtractor. The best results have been obtained performing a background estimation with a mesh of $13.5^{'} \times 13.5^{'}$. After the background subtraction, the map has been convolved with the optimal MHW provided by SExtractor. We have checked that a gaussian filter works worse than the MHW. The results, for the minimum flux reached in our method (applying first criterion), are: 74 point sources detected using SExtractor, with a mean error of 29.02% and 68 ones detected using our technique, with a mean error of 8.83%. SExtractor can detect 6 point sources more than our method, but these detections have a large error. In fact, a high number of the SExtractor detections have an error $> 100\%$, especially for low amplitude point sources. We reject this spurious detections in our method because of the scale fit used. We have also compared the

results for the completeness flux. In this case, we can reach a slightly lower flux than SExtractor, and the results are: 35 point sources detected using SExtractor, with a mean error of 14.41% and 43 ones using our method, with a mean error of 4.95%. We want to remark that the map analysed is the most suitable case for the SExtractor performance. The power of our method is not only supported by the choice of the MHW as filter, but also by the study of the optimal scale and the scale fit. This allows us to optimize both the detection and the amplitude estimation, as well as to reject spurious detections.

The MHW method works better at high frequencies. Dust is dominating the maps at those frequencies, having a *coherence scale* greater than the antenna beam (point source scale). However, at low frequencies the main background is CMB, whose *coherence scale* is similar or lower than the antenna dispersion. In this situation both point sources and background have a similar variation scale. We have proved that an optimal selection of the MHW scale is important in order to reach high amplifications. We must study each image separately and, in particular, we need to compute the power spectrum from each image in order to calculate the wavelet coefficient dispersion for several MHW scales and look for the maximum amplification.

In those cases where the background has a similar variation scale than the point sources or it has a high emission, the MHW tends to an optimal scale lower than the antenna dispersion. On the other hand, on those patches having a background with a variation scale greater than the point sources (usually dust emission at high frequencies) we are able to detect a large number of point sources and we can reach very low levels; in this case the analysing scale of the MHW should be greater than the antenna dispersion. At this point, the noise (with pixel scale variation) plays a very important role and makes the MHW take this relatively large optimal scale. Therefore, given a particular image, the optimal MHW scale arises from a compromise between the intensity and *coherence scale* of the dominant foreground (or CMB background) and the noise amplitude.

One could think in different ways of improving the number of detections. Denoising the maps before applying the detection method could be important to increase the number of point sources detected in those maps where the noise is the main problem: in the high frequency channels. The denoising method should be such that it preserves the Gaussian shape of point sources in order to preserve the efficiency of the MHW.

The antenna size also plays an important role since it is limiting the number of point sources detected at frequencies at which the CMB is the dominating signal. Only a better angular resolution at low frequencies (below the CMB *coherence scale*) could improve the number of detections. In this case (and also in the previous one) we can increase the number of detections using the information about the spectral index of the point source families we have detected. Another way to improve both the number of detections and the amplitude estimation would be to combine the MHW method with the MEM one. Since the last one has problems in subtracting the brightest sources in the maps, the MHW would represent a natural complement to MEM. A collaborative effort in this direction is being carried out at present (Vielva et al. 2000).

A generalization of the method to account for possible elliptical asymmetries in the gaussian beam profile can be easily done by modifying the isotropic MHW to have the same asymmetry. However, in the specific case of the Planck mission an important effort is presently being done in order to avoid beam asymmetries. Otherwise, due to the scanning strategy which will cover the entire sky with circles, small asymmetries would imply a strong degradation of the data.

In the near future we plan to implement the MHW method to work directly on maps covering the whole sphere, using the pixelization adopted by Planck. All sky point source simulations will clearly allow for the presence of brighter sources than considered in this work. These sources will be easily detected by the MHW method.

Finally we would like to emphasize that the MHW method will allow for a direct extraction of the *Planck Extragalactic Point Source Catalogue* before any foreground removal or separation is done. The catalogue will be obtained with amplitude estimation errors below 15%. This will be of great value, not only increasing the number of extragalactic sources known at Planck frequencies but also providing information about the spectral behaviour of different populations, among which there is an important lack of knowledge at present.

ACKNOWLEDGMENTS

We thank B. Guiderdoni for kindly providing us with the source counts predicted by his model E. We also thank B. T. Draine and A. Lazarian for providing us with the emissivity predicted by their spinning dust model. We thank Julio Gallegos for his help with synchrotron emission simulations and Luis Tenorio and Diego Herranz for useful comments. We also thank R. F. Bouchet for helpful suggestions and comments. PV acknowledges support from Universidad de Cantabria fellowship as well as the CfPA hospitality during November 1999. JMD acknowledges support from a Spanish MEC fellowship FP96 20194004. We thank the Comisión Conjunta Hispano–Norteamericana de Cooperación Científica y Tecnológica ref. 98138, Spanish DGESIC Project no. PB98-0531-c02-01 for partial financial support. EMG, LC and JLS thank FEDER Project no. 1FD97-1769-c04-01 for partial financial support. EMG, LC, JMD and JLS thank the EEC Project INTAS-OPEN-97-1992 for partial financial support.

REFERENCES

Aghanim, N. & Forni, 0., 1999, A&A, 347, 409.

Baccigalupi, C., Bedini, L., Burigana, C., De Zotti, G., Farusi, A., Maino, D., Maris, M., Perrota, F., Salerno, E., Toffolatti, L., Tonazzini, A., 2000, astro-ph/0002257

Bouchet, F. R., Gispert, R. & Puget, J. L., 1996 in Drew, E., ed., Proc. AIP Conf. 384, The mm/sub-mm foregorunds and future CMB space missions. AIP Press, New York, p. 255

Bouchet, F. R., Prunet, S. & Sethi, S. K., 1999, MNRAS, 302, 663

Boulanger, F. & Pérault, M., 1988, ApJ, 330, 964.

Cayón, L., Sanz, J. L., Barreiro, R. B., Martínez-González, E., Vielva, P., Toffolatti, L., Silk, J., Diego, J. M. & Argüeso, F., 2000, C00, MNRAS, 315, 757.

Diego, J. M., Martínez-González, E., Sanz, J. L., Cayón, L. & Silk, J., 2000, MNRAS submitted.
Draine, B. T. & Lazarian, A., 1998, ApJ, 494, L19.
Ferreira, P, Magueijo, J. & Silk, J., 1997, Phys. Rev. D, 56, 4592.
Finkbeiner, D. P., Davis, M. & Schlegel, D. J., 1999, ApJ, 524, 867
Guiderdoni, B., Hivon, E., Bouchet, F. R. & Maffei, B., 1998, MNRAS, 295, 877
Haslam, C. G. T., Salter, C. J., Stoffel, H. & Wilson, W. E., 1982, A&AS, 47, 1
Hobson, M. P., Jones, A. W. Lasenby, A. N. & Bouchet, F. R., 1998, MNRAS, 300, 1
Hobson, M. P., Barreiro. R. B., Toffolatti, L., Lasenby, A. N., Sanz, J. L., Jones, A. W. & Bouchet F. R., 1999, MNRAS. 306, 232.
Jonas, J. L., Baart, E. E. & Nicolson, G. D., 1998, MNRAS, 297, 977
Mandolesi, N. et al. 1998: Proposal submitted to ESA for the Planck Low Frequency Instrument.
Puget, J. L. et al. 1998: Proposal submitted to ESA for the Planck High Frequency Instrument.
Reich, P. & Reich, W., 1986, A&AS, 63, 205
Sanz, J. L., Argüeso, F., Cayón, L., Martínez-González, E., Barreiro, R. B. & Toffolatti, L., 1999a, MNRAS, 309, 672.
Sanz, J. L., Barreiro, R. B., Cayón, L., Martínez-González, E., Ruiz, G. A., Díaz, F. J., Argüeso, F., Silk, J. & Toffolatti, L., 1999b, A&AS, 140, 99.
Sanz, J. L., Herranz, D. & Martínez–González, E., 2000, ApJ, accepted.
Seljak, U. & Zaldarriaga, M., 1996, ApJ, 469, 437.
Tegmark, M. & Oliveira-Costa, A., 1998, TOC98, ApJ, 500, 83.
Tenorio, L., Jaffe, A. H., Hanany, S. & Lineweaver, C. H., 1999, MNRAS, 310, 823.
Toffolatti, L., Argüeso, F., De Zoti, G., Mazzei, P., Franceschini, A., Danese, L. & Burigana, C., 1998, MNRAS, 297, 117.
Vielva, P., Barreiro, R. B., Hobson, M. P., Martínez–González, E., Lasenby, A. N., Sanz, J. L. & Toffolatti, L., 2000, MNRAS, submitted.

This paper has been produced using the Royal Astronomical Society/Blackwell Science LaTeX style file.